

# Supernova Remnants in the Large Magellanic Clouds IX: Multiwavelength Analysis of the Physical Structure of N49

J. Bilikova, R. N. M. Williams, Y.-H. Chu, R. A. Gruendl and B. F. Lundgren

*Astronomy Department, University of Illinois at Urbana-Champaign  
1002 W. Green St. Urbana, IL 61801*

## ABSTRACT

We present a multiwavelength analysis of the supernova remnant N49 in the Large Magellanic Cloud. Using high-resolution *Hubble Space Telescope* WFPC2 images of  $H\alpha$ , [S II] and [O III] emission, we study the morphology of the remnant and calculate the rms electron densities in different regions. We detect an offset of [O III] and  $H\alpha$  emission peaks of about  $0''.5$ , and discuss possible scenarios that could give rise to such high values. The kinematics of the remnant is analyzed by matching individual kinematic features in the echelle spectra obtained at CTIO with the morphological features revealed in the WFPC2 images. We detect narrow  $H\alpha$  emission component and identify it as the diffuse pre-shock recombination radiation, and discrete broad emission features that correspond to the shocked gas in filaments. The overall expansion of the remnant is about  $250 \text{ km s}^{-1}$ . The dense clouds are shocked up to line-of-sight velocities of  $250 \text{ km s}^{-1}$  and the less dense gas up to  $300 \text{ km s}^{-1}$ . A few cloudlets have even higher radial velocities, reaching up to  $350 \text{ km s}^{-1}$ . We confirm the presence of the cavity in the remnant, and identify the center of explosion. Using archival *Chandra* and *XMM-Newton* data, we observe the same trends in surface brightness distribution for the optical and X-ray images. We carry out the spectral analysis of three regions that represent the most significant optical features.

*Subject headings:* ISM: individual(N49) – supernova remnants – X-rays: individual(SGR 0526-66)

## 1. Introduction

N49 is the most optically bright supernova remnant (SNR) in the Large Magellanic Cloud (LMC). In contrast to a classic shell-type SNR, N49 exhibits largely asymmetric morphology at optical wavelengths. The increased brightness of this SNR in the southeast

and its unique filamentary structure at optical wavelengths has long set N49 apart from other well-understood SNRs. Inhomogeneities in the optical morphology and kinematics of N49 have been observed in the past (Shull 1983; Chu & Kennicutt 1988; Vancura et al. 1992a). However, the fine structure resolved from these kinematic observations was difficult to reconcile with the optical images taken from the ground. Recent mapping of molecular clouds in the region suggests that this SNR is expanding into a denser region toward the southeast, which has caused the asymmetric brightness enhancements in the shell (Banas et al. 1997).

The presence of such a filamentary structure suggests that dense material surrounded the progenitor star at the time of its supernova. In the case of a massive progenitor star, its strong stellar wind would have cleared most material from the environment during its lifetime. Considering the evidence for a relatively dense environment surrounding N49, a B-type star, which would lack a strong stellar wind, is the most likely candidate for the N49 progenitor (Shull 1983).

This SNR also appears notably bright at the X-ray (Williams et al. 1999; Park et al. 2003) and radio (Dickel et al. 1995) wavelengths, in which the complete spherical shell of the remnant is clearly visible. While the overall structure appears symmetric at X-ray wavelengths, the brightness peaks in the southeastern region as in the optical. In the *Chandra* observations, most of the optically bright filamentary structures have only diffuse X-ray counterparts. These observations also revealed a hard X-ray knot extending beyond the main shell in the southwest of N49, which has been suggested to be a fragment of the explosion accelerated beyond the shock boundary.

An additional point of interest is the existence of a known soft gamma-ray repeater, SGR 0526-66, within the boundary of N49. Recent *Chandra* images have resolved a point source, suggested to be the X-ray counterpart to this SGR (Kulkarni et al. 2003). No optical or radio counterparts of this SGR have been detected (Dickel et al. 1995; Smith et al. 1998; Fender et al. 1998), and the SGR does not seem to have strong influence on the overall optical morphology of the remnant.

In order to understand the kinematics of the remnant and the distribution of X-ray emission in terms of the detailed physical structure of the N49 SNR, we have obtained high-resolution *Hubble Space Telescope* (*HST*) images in the  $H\alpha$ , [O III], and [S II] emission lines, which reveal N49's bright filamentary structures with high precision. We have supplemented existing high-dispersion spectroscopy (Chu & Kennicutt 1988) with additional deep spectra for N49 to investigate the full extent of velocity distribution. In this paper, we analyze the above observations in conjunction with archival *Chandra* and *XMM-Newton* observations for a comprehensive multi-wavelength study of the physical structure of N49. §2 describes the

included observations, §3 analyzes the *HST* emission line images and the implications of the surface brightness and the line ratios, §4 analyzes the nebular kinematics and correlates the kinematic and morphological features, and §5 compares the X-ray and optical morphologies and discusses the relative distribution of hot and cool gas, and a summary is given in §6.

## 2. Observations

### 2.1. Optical Emission-Line Images

We imaged N49 using the *HST* Wide Field Planetary Camera 2 (WFPC2) with three filters: F656N ( $H\alpha$ ), F673N ( $[S\ II]\ \lambda\lambda 6717, 6731$ ) and F502N ( $[O\ III]\ \lambda 5007$ ). The dates and exposure times of these observations are presented in Table 1. The data were reduced using the STSDAS package within IRAF<sup>1</sup>. The continuum was not subtracted, as the line emission was so dominant that the presence of continuum would not affect our conclusions. Cosmic-ray events were removed by combining multiple exposures, and the resulting files were bias-subtracted. Each image was divided by its exposure time to produce a count-rate map. These maps in turn were multiplied by a conversion factor, given by the PHOTFLAM parameter in the image header, to produce flux-density maps. We used the SYNPHOT task to determine widths for each filter, and multiplied the flux-density maps by the corresponding filter widths to produce flux maps. The resulting files were then mosaicked together for the final images.

### 2.2. Optical Spectroscopy

We obtained high-dispersion spectra of N49 with the echelle spectrograph on the Blanco 4m telescope at Cerro Tololo Inter-American Observatory (CTIO) in three observing runs. A journal of our observations is given in Table 2. We used the 79 line  $\text{mm}^{-1}$  echelle grating in the single-order, long-slit observing configuration, with a flat mirror replacing the cross disperser and a post-slit  $H\alpha$  filter ( $\lambda_c = 6563\ \text{\AA}$ ,  $\Delta\lambda = 75\ \text{\AA}$ ) inserted to isolate a single order.

Due to the vignetting limitations imposed by the optics, the useful spatial coverage is  $\sim 3'$ . The spectral coverage includes both the  $H\alpha$  line and the neighboring  $[N\ II]\ \lambda\lambda 6548, 6583$  lines. We used a slit width of  $250\ \mu\text{m}$  ( $1''64$ ) for all observations. The spectral dispersion and

---

<sup>1</sup>Image Reduction Analysis Facility, maintained by NOAO

wavelength were calibrated by a Th-Ar lamp exposure taken in the beginning of each night, and fine-tuned using the geocoronal H $\alpha$  and telluric OH lines present in the echellograms.

The 1986 observing run used the Air Schmidt camera and a GEC 385 $\times$ 586 CCD. The 22  $\mu\text{m}$  pixel size corresponds to about 0.21  $\text{\AA}$  and 0'635 along the dispersion and spatial axes, respectively. The instrumental profile had a FWHM of  $21 \pm 0.5 \text{ km s}^{-1}$ , as measured from the Th-Ar calibration and sky lines. The echelle spectra obtained in this observing run have been reported by Chu & Kennicutt (1988).

The 1995 observing run used the red long-focus camera and a Tek 2048 $\times$ 2048 CCD. The 24  $\mu\text{m}$  pixel size corresponds to roughly 0.082  $\text{\AA}$  and 0'26 along the dispersion and spatial axes, respectively. The instrumental profile had a FWHM of  $16.1 \pm 0.8 \text{ km s}^{-1}$ .

The observations made in 2000 were recorded using the red long-focus camera and the SITe2K#6 2048 $\times$ 2048 CCD. The 24  $\mu\text{m}$  pixel size corresponds to roughly 0.082  $\text{\AA}$  and 0'26 along the dispersion and spatial axes, respectively. The instrumental profile had a FWHM of  $13.5 \pm 0.5 \text{ km s}^{-1}$ .

### 2.3. X-ray Images and Spectroscopy

X-ray observations of N49 were made with both the *XMM-Newton* and *Chandra* observatories. We retrieved the pipeline-processed *XMM-Newton* data from the Science Operations Centre (SOC). Observations were made simultaneously with multiple *XMM-Newton* instruments; in this paper we will concentrate on the European Photon Imaging Camera (EPIC) MOS and pn detectors. The data were taken in 2001 April (Observation ID 0113000201; 26.9 ks; PI: Kaastra) over multiple time intervals, using the Thick filter for two EPIC-MOS1 exposures and the Medium filter for the remaining EPIC-MOS and EPIC-pn exposures. Initial reduction and analysis were carried out using the Science Analysis Software package provided by the SOC, with subsequent spectral analysis in XSPEC.

The data were filtered to remove high background times or poor event grades and merged to produce a single dataset for each instrument with effective exposure times of 14.3 ks for EPIC-MOS1, 19.5 ks for EPIC-MOS2 and 0.8 ks for EPIC-pn. Images were then extracted from the filtered merged event files. Spectra were extracted separately from each exposure, to avoid introducing distortions due to the different filters used. Background regions immediately surrounding the SNR but free of point sources were used to produce background spectra, which were then scaled and subtracted from the source spectra. Spectra from different exposures were jointly fitted.

*Chandra* observations used the Advanced CCD Imaging Spectrometer (ACIS), primarily the S3 back-illuminated chip. Datasets were sequence number 500107, observation 1041 (34.3 ks; PI: Garmire) and sequence number 500134, observation 2515 (7.0 ks; PI: Kulkarni). Data were reprocessed following procedures recommended by the Chandra X-ray Center: we removed afterglow corrections, generated new bad pixel files, and applied corrections for charge-transfer inefficiency and time-dependent gain for an instrument temperature of 120 K. The two datasets were filtered for high-background times and poor event grades, resulting in total “good time” intervals of 33.9 and 6.9 ks.

Spectral results were extracted from the new event files. Background regions were taken from source-free areas surrounding the SNR, and the spectra of these background regions were scaled and subtracted from the source spectra. Individual spectra for regions of interest, selected by comparison of optical and X-ray images, and the corresponding primary and auxiliary response files were extracted with the CIAO `acisspec` script and analyzed in XSPEC. Spectra were rebinned by spectral energy to achieve a signal-to-noise ratio of 4 in each bin.

### 3. Analysis of the HST Emission Line Images

#### 3.1. H $\alpha$ Surface Brightnesses and Electron Densities

The *HST* H $\alpha$  image (Fig. 1a) displays a complex network of filaments with the brightest emission located toward the southeast. In Figure 1b, we have marked the morphological features of the remnant, which will henceforward be referred to as features i to vi. The most prominent feature is the SE Ridge (feature i), a ridge of bright filaments in the southeast quadrant, tracing a line from east to south of the SNR. From the SE Ridge, straight bright filaments extend toward the northwest over lengths of 15–30'' (ii). A network of bright filaments is present in the southwestern part of the remnant (iii), where the filaments are shorter than those in the SE Ridge. Beyond this network toward the outer edge of the remnant, there exist a number of fainter filaments (iv). Faint filaments are also seen in the northern and northeastern parts of the SNR (v). No bright filaments exist in the western part of the remnant.

The bright filaments are enveloped by a diffuse H $\alpha$  emission component. This diffuse emission extends beyond the radio/X-ray (Williams et al. 1999; Park et al. 2003; Dickel et al. 1995) boundary along the circumference from the north through the east to the south. On the west side of the remnant, only faint patches of H $\alpha$  emission exist (feature vi). While the outermost emission patches follow the X-ray/radio boundary, they do not appear to be

embedded in a diffuse emission component, which is either absent or below the detection limit.

Due to its presence beyond the shock boundary, we identify the diffuse H $\alpha$  emission as the recombination radiation of hydrogen ionized by the UV precursor in the pre-shock region.

The H $\alpha$  surface brightness ( $SB$ ) of a  $10^4$  K ionized gas can be expressed as

$$SB = 1.9 \times 10^{-18} n_e^2 L_{pc} \text{ ergs s}^{-1} \text{ cm}^{-2} \text{ arcsec}^{-2}, \quad (1)$$

where  $n_e$  is the electron density in  $\text{cm}^{-3}$  and  $L_{pc}$  is the emitting path length in pc. Using the flux-calibrated *HST* H $\alpha$  image<sup>2</sup> and reasonable estimates of the emitting path lengths, we may determine the gas densities. For a filament, we adopt its length as upper limit and its width as lower limit for the emitting path length. For a diffuse emission region, we adopt its average diameter as the emitting path length.

In the brightest filaments, such as the SE Ridge, the long filaments extending to the northwest, and the bright short filaments in the southwest,  $SB$  is  $\sim (1 \pm 0.4) \times 10^{-13}$  ergs  $\text{s}^{-1} \text{cm}^{-2} \text{ arcsec}^{-2}$ , with the peak emission reaching  $2 \times 10^{-13}$  ergs  $\text{s}^{-1} \text{cm}^{-2} \text{ arcsec}^{-2}$ . The rms densities in these bright filaments are between the limits of  $265 \pm 20$  and  $515 \pm 20$   $\text{cm}^{-3}$ , adopting the length and width of the filaments as the emitting path lengths, respectively.

The filaments in the central and northeastern regions, as well as the brighter northern filaments, are slightly fainter than the SE Ridge, with  $SB$  of  $(3 - 8) \times 10^{-14}$  ergs  $\text{s}^{-1} \text{cm}^{-2} \text{ arcsec}^{-2}$ . The rms electron densities in these filaments are between the limits of  $115 \pm 20$  and  $310 \pm 20$   $\text{cm}^{-3}$ . The  $SB$  of the fainter filaments in the remnant, such as the northernmost filaments, is  $(0.9 - 2) \times 10^{-14}$  ergs  $\text{s}^{-1} \text{cm}^{-2} \text{ arcsec}^{-2}$ . The rms densities here are between the limits of  $70 \pm 20$  and  $225 \pm 25$   $\text{cm}^{-3}$ .

The faint patches in the western quadrant have  $SB$  of  $(1-4) \times 10^{-15}$  ergs  $\text{s}^{-1} \text{cm}^{-2} \text{ arcsec}^{-2}$ . Adopting their average diameters as the emitting path lengths, the rms densities in the patches are  $90 \pm 10$   $\text{cm}^{-3}$ . The diffuse H $\alpha$  emission that envelops the bright filaments has a similar  $SB$ , but a larger emitting path length. Approximating the emitting path length by the radius of the remnant, we get rms densities of about  $10 \pm 5$   $\text{cm}^{-3}$ .

Our derived rms densities are significantly lower than the densities of  $1000 - 1800$   $\text{cm}^{-3}$  calculated using the [S II] doublet ratios reported by Vancura et al. (1992b). This difference can be explained by the different weightings placed on density by these two methods. The

---

<sup>2</sup>The WFPC2 H $\alpha$  filter (F656N) also transmits the [N II]  $\lambda 6548$  line, which is  $\sim 8\%$  as bright as the H $\alpha$  line in N49 (Vancura et al. 1992b). This [N II] contamination has been corrected for.

flux of an emission line is proportional to  $\int n_e^2 dL$ , thus an over-dense region along a line of sight will dominate the emission and dictate the electron density determined from the [S II] doublet ratio. On the other hand, the rms density is derived from the emissivity averaged over the entire emitting path length, and therefore is always lower than the peak value determined from the [S II] doublet. In general, the density determined from the [S II] doublet is representative of the densest regions, while the rms density better represents the density over the entire emission path length. The rms densities are particularly useful for region whose density is  $< 100 \text{ cm}^{-3}$ , the low-density limit of the [S II] doublet, such as the faint emission regions.

### 3.2. [S II] Emission and [S II]/H $\alpha$ Ratios

Overall, the morphology of N49 in the [S II] line (Fig. 1c) resembles that in the H $\alpha$  line. For example, the bright SE Ridge, the straight bright filaments extending to the northwest, the fainter filaments in the north and west, and the faint emission patches in the west are all observed in the [S II] image. The most notable morphological difference between the [S II] and H $\alpha$  images is the lack of a diffuse [S II] emission component enveloping the bright filaments.

As the morphologies of N49 in the H $\alpha$  and [S II] lines are similar, the ratio map (Fig. 1d) is fairly uniform, with a mean value of  $0.75 \pm 0.05$ . However, there are variations in this ratio, giving an overall range of 0.4 – 1.4. These variations result from different shock conditions. The highest ratios are found in the bright filaments extending northward from the SE Ridge, where the ratios reach values of 1 – 1.4. The lowest ratios can be seen in the outermost limb of the remnant, where the ratios are below 0.4, which may be due to the lack of a diffuse [S II] component. In addition, we find low ratios in the SE Ridge, where the H $\alpha$  filaments are the brightest.

### 3.3. [O III] Emission and [O III]/H $\alpha$ Ratios

The [O III] emission (Fig. 1e) is filamentary and peaks in the southeast just like the H $\alpha$  and [S II], but the filamentary structures differ in details. The [O III] emission associated with bright H $\alpha$  and [S II] filaments is usually concentrated in faint thin filaments and shows an offset toward the leading edge of the shock fronts. The most extreme difference is exhibited in the bright H $\alpha$  filament extending from the northern tip of the SE Ridge toward northwest, where the [O III] emission is absent.

These and other morphological differences are best demonstrated by the [O III]/H $\alpha$  ratio map (Fig. 1f). The ratios generally increase from the inner to the outer part of the remnant, spanning a wide range from nearly 0 to about 2.5. The ratios in the inner portions of the remnant range from 0 to about 0.5, with a few regions reaching ratios of 0.7. The ratio map in the inner portions of the remnant shows a filamentary structure that is not as sharp as the direct images. The brighter and fainter “filaments” on the ratio map have values of 0.4 – 0.7, and 0.05 – 0.15, respectively. Generally, the filaments bright in H $\alpha$  have very low [O III]/H $\alpha$  ratios. This can be seen in the SE Ridge, where the brightest H $\alpha$  filaments are faint on the ratio map. Ratios above 0.5 are found primarily in the outer portions of the remnant. The most prominent feature of the ratio map is the increase in the ratios toward the outermost edge of the remnant, where they reach values between 0.8 and 1.5. A few small patches in the north, northeast and southwest reach the values of up to 2.5 on their outer edge.

The enhanced [O III]/H $\alpha$  ratios at the edges of the SNR appear to be at least as much due to a diminishment in the H $\alpha$  emission as to an increase in [O III] emission. This morphology demonstrates an offset of [O III] emission toward the outer edge of the remnant, seen also in the composite image of H $\alpha$ , [S II] and [O III] emission (Fig. 4b). We evaluate the offset by comparing the peaks of brightness profiles across the filaments in [O III] and H $\alpha$ . Sample SB profiles demonstrating this offset are shown in Fig. 2. We find the offsets to range from 0 up to  $\sim 0''.5$ , or 0.125 pc (for a distance of 50 kpc; Feast 1999).

On small scales, we would expect an offset between the [O III] and H $\alpha$  filaments because the emissivity and ionic concentration of a given line depend on the temperature and thus the distance from the shock front. In a plain, steady-shock model, the hydrogen recombination emission peaks roughly where [O III] and [O II] emission diminishes and [O I] emission rises (Cox 1972). The time scale needed for a post-shock region to evolve from [O III]-bright to [O III]-faint is  $\sim 2000/n_0$  yr, where  $n_0$  is the pre-shock density in units of H-atom  $\text{cm}^{-3}$  (Raymond et al. 1980). Therefore, we expect the post-shock [O III] emission peak and the H $\alpha$  emission peak to exhibit a displacement of  $v \times (2000\text{yr}/n_0)$ , where  $v$  is the velocity of the post-shock gas with respect to the shock front. In case of an adiabatic (Sedov) shock, the post-shock gas expands downstream with  $\frac{1}{4}$  of the shock velocity; thus the shocked gas in the clouds is observed to move with  $v_c = \frac{3}{4}v_s$ , where  $v_s$  is the shock speed.

For a dense cloud with  $n_0 = 1000 \text{ cm}^{-3}$  (the lower limit for the filament density calculated by Vancura et al. (1992b)), with an observed expansion velocity  $v_c = 250 \text{ km s}^{-1}$ , the displacement between [O III] and H $\alpha$  will be  $1.7 \times 10^{-4}$  pc, or  $0''.0007$ , which cannot be resolved by the *HST*. For the shock with the same velocity driven into the diffuse regions of N49, where the density is about  $n_0$  of  $10 \text{ cm}^{-3}$ , the offset between [O III] and H $\alpha$  can be

raised to 0.017 pc, or 0''.07. This value still cannot be resolved by the *HST*.

There are several other scenarios that would produce an offset between [O III] and H $\alpha$  emission, each involving a departure from a steady-flow shock model. Using observations from the MagIC camera at the Clay Telescope, Rakowski et al. (2007) compared the locations of the [OIII] and H $\alpha$  peaks, finding separations of up to 0''.62. Our HST observations, which do not suffer from seeing distortions, show peak separations of up to 0''.5. Rakowski et al. (2007) attributed these offsets to thermal instabilities dampened by magnetic field, following the models of Innes (1992), who associates the offsets with the presence of secondary shocks. These models have predicted maximum offsets of  $3 \times 10^{17}$  cm, which for the distance of the LMC yields roughly 0''.4 (Rakowski et al. 2007). However, the physical conditions for the models ( $v_s=175$  km s $^{-1}$ ,  $n_0 = 1$  cm $^{-3}$ ,  $B_0 = 3$   $\mu$ G) are different from the ones in the LMC. As Rakowski et al. (2007) point out, the abundances of the LMC will increase the cooling time by a factor of 3, which would tend to increase the offset by this factor. Our derived pre-shock density is 10 cm $^{-3}$ , which is 10 times higher than the value used for the models, so the net result of these 2 effects is a decrease in the offset by a factor of 10/3, giving an offset of roughly 0''.15. Rakowski et al. (2007) argued that the fast shocks seen in N49 made this the most probable scenario. However, without a substantial amount of magnetic support, the derived values are still smaller than the maximum observed offsets.

An alternate scenario was presented by Raymond et al. (1980, 1983) for such offsets in the Cygnus Loop. In this scenario, the offsets arise due to incomplete recombination zones behind a shock front driven into an inhomogeneous environment. For a SNR in a cloudy medium, the slow shocks driven into dense clouds produce the [O III] and H $\alpha$  emission, while the fast shocks propagating into the less-dense intercloud medium produce X-ray emission. The H $\alpha$  and [O III] lines are both emitted from shocked dense clouds, but their “turn-on“ times are different by  $\sim 2000/n_0$  yr. As the fast shocks advance through the intercloud medium and encounter clouds, [O III] emission will be produced almost immediately in the freshly shocked clouds, and the H $\alpha$  emission is produced by clouds that were shocked  $\sim 2000/n_0$  yr earlier. The displacement between the [O III] and H $\alpha$  peaks is thus  $\sim (v_{s,i} - v_{s,c}) \times 2000\text{yr}/n_0$ , where  $v_{s,i}$  is the velocity of a fast shock through the intercloud medium and  $v_{s,c}$  is the velocity of a slow shock through a dense cloud (Fesen et al. 1982).

The velocity of the fast shock in the intercloud medium can be estimated from the temperature of the post-shock, X-ray emitting gas, using

$$kT = \frac{3}{16} \mu m_{\text{H}} v_{s,i}^2, \quad (2)$$

where  $m_{\text{H}}$  is the mass of the hydrogen atom and  $\mu$  is the mean molecular weight. For a fully ionized gas with He:H = 1:10,  $\mu$  is 0.6. Adopting the higher temperature component  $kT =$

1.0 keV (Park et al. 2003), we get a  $v_{s,i} = 920 \text{ km s}^{-1}$ . The highest velocities seen in the dense shocked clouds, obtained from the echelle spectra (see §4.), are about  $250 \text{ km s}^{-1}$ . The post-shock gas in the clouds was accelerated to  $0.75v_{s,c}$ . The pre-shock density is  $10 \text{ cm}^{-3}$ . Therefore, the expected displacement between the [O III] and  $\text{H}\alpha$  peaks is 0.12 pc, or  $0''.5$ . This offset is in excellent agreement with the observation.

#### 4. Analysis of Filament Velocity Structure with Echelle Spectra

To determine the exact slit positions of the echelle observations, we match the  $SB$  profiles along the slit to those extracted from the  $HST$   $\text{H}\alpha$  image. The high angular resolution of the  $HST$  images allows us for the first time to see one-to-one correspondence between the kinematical and morphological features of N49 (Fig. 3).

##### 4.1. Discrete Features

The echellograms in Figure 3 show discrete broad emission features as well as a narrow component extending continuously along the slit. The narrow component, detected by Chu & Kennicutt (1988) and Vancura et al. (1992b) shows  $SB$  enhancements within the boundary of the SNR, indicating physical association; we therefore adopt its heliocentric velocity ( $v_{\text{hel}}$ ) of  $315 \text{ km s}^{-1}$  as the SNR’s systemic velocity. Due to our extended slit coverage, we are able to pin down the location of this enhanced narrow component in the SNR. The  $SB$  variation of this narrow component is similar to that of the diffuse  $\text{H}\alpha$  emission, brighter in the east and fainter in the west. We therefore associate this narrow component with the faint diffuse  $\text{H}\alpha$  component identified morphologically in §3.1. The narrow velocity width and the pre-shock location of this narrow component are consistent with its origin as recombination radiation of hydrogen ionized by the UV precursor of the SNR shocks.

We also observe broad emission features which indicate the bulk expansion of about  $250 \text{ km s}^{-1}$ . Some of the broad emission features have a “head-tail” structure; the bright emission at a head has a smaller radial velocity offset ( $\Delta v$ ) from the systemic velocity and the fainter emission in the tail stretches to larger  $\Delta v$ . Among the discrete broad emission features, the brighter ones have smaller  $\Delta v$ , ranging from 0 to  $160 \text{ km s}^{-1}$  at the “head” and up to about  $250 \text{ km s}^{-1}$  at the “tail”. They can be well matched to individual bright filaments.

The structure of these emission features can be explained by the interaction between the shock and the encountered dense gas. The shock gets dampened more by the dense gas in the

filaments than in the lower-density cloudlets. Therefore, the post-shock gas in the inner part of the dense bright regions was propelled to velocities significantly lower than the original shock velocity, thus producing smaller velocity spreads. The presence of gas at systemic velocity suggests that the gas in these regions retarded the shock sufficiently to prevent its propagation throughout the whole filament, leaving the innermost gas unshocked. Because it emits the  $H\alpha$  recombination radiation, it must have been ionized by the UV precursor. The fainter “tail” emission comes from the outer layers of these dense filaments that encountered the undampened shock and have been accelerated to higher velocities.

The less dense gas, which can be identified on echelle spectra as fainter emission component, can be accelerated by the shock to very high velocities. The lower-density gas is unable to significantly slow down the shock, and the post-shock gas is consequently accelerated to higher speeds. We observe velocity spreads of up to  $300 \text{ km s}^{-1}$ . Some of these cloudlets have no systemic velocity components, which implies that all of the gas is shocked.

A few cloudlets have velocity spreads that exceed  $300 \text{ km s}^{-1}$ . One example is a faint emission knot seen at the edge of the remnant in observation E2000-1, which has been marked in Figure 3 as feature a. The clump has a radial velocity spread of  $350 \text{ km s}^{-1}$ . Due to its location at the edge of the remnant, it likely has a significant tangential velocity component and thus the actual velocity of the blob is even higher. Assuming the two components to be comparable, the actual velocity of some of the gas in this blob could be up to  $\sim 500 \text{ km s}^{-1}$ .

## 4.2. Overall Kinematic Structure

The observed distinct broad emission features have implications for the physical structure of the SNR. The echelle spectra do not suggest the presence of an expanding shell, which would demonstrate itself as a simple bow-shaped line image. The absence of this expanding shell signature in the echelle spectra implies that the observed filaments are not projection effects of an expanding sheet of gas, but actual long ribbon-like structures which indicate clumpiness in the surrounding gas prior to the explosion.

We have taken echelle spectra in the southern part of the remnant (E2000-2, E2000-3) to see whether the arc-like filament in the south is Balmer line dominated. We can however observe  $[\text{N II}] \lambda 6584$  line in the spectra, and thus conclude that the arc is not Balmer dominated.

In observations E1986-2 and E2000-1, we observe very few broad component features at systemic velocity around the center of explosion determined from X-ray and radio data. In the blueshifted part of the echelle spectra, we see no broad features at all in E1986-2,

and only few faint ones in E2000-1. In the redshifted part, we observe a number of broad features in both spectra, but only one of these in E2000-1 has the lower end of its velocity spread at the systemic velocity. The rest of the broad features are seen at higher velocities. Such spectra suggest the presence of a central cavity; its position matches the X-ray and radio observations. The asymmetry of the emission in this central region implies uneven density distribution of matter prior to the explosion, with higher density at the far side of the remnant.

The comparison of the echelle spectra with optical morphology of the SNR allows us to see three-dimensional geometry of the remnant. Using the echelle spectra, we were able to discern whether individual filaments are on the approaching or the receding side of the remnant. Assigning blue and red colors to the blue- and redshifted filaments, respectively, we have constructed a 3D image of N49 (Fig. 4a). For the most part, we see the near and the far side of the remnant superimposed, but we observe a number of prominent red and blue filaments. The most prominent redshifted filaments are the straight long filaments extending from the SE Ridge northwards. The majority of the outer filaments is blueshifted, for example a filament extending westward from the SE Ridge.

## 5. Comparison of X-ray and Optical Morphology

To better trace the relationship of the warm ionized gas in the optically-emitting filaments with the hot shocked gas, we compared the *HST* images with data from *XMM-Newton* and *Chandra*. All of the X-ray images show a bright, point-like X-ray source to the north corresponding to the location of the soft gamma-ray repeater SGR 0525-66, as noted by Rotschild, Kulkarni & Lingenfelter (1994). This bright source appears between optically bright features, in a relatively void optical region, and it is not associated with any optical source.

The X-ray image of N49 from *XMM-Newton* is presented in Figure 5a. The corresponding X-ray contours are overlaid on the  $H\alpha$  observation from *HST* in Figure 5b. The  $2\sigma$  contour provides a nicely defined boundary to the expanding shell. In general, the comparison of *XMM-Newton* and optical images reveals a strong relationship between X-ray brightness and the regions of highest optical flux. As with the optical brightness, the X-ray flux declines toward the west, although the western side of the SNR is still detectable. To the southeast, the steeper X-ray contours indicate a substantial X-ray brightening corresponding to the bright SE ridge in optical; this emission appears to be resolved without any obvious point source. Westward from this X-ray peak, the central cavity described in the velocity structure analysis (§4) appears somewhat brighter in X-rays than do regions to the west and

north of the SNR.

A recent short *Chandra* exposure enables an X-ray/optical comparison at higher resolution. The X-ray image of N49 from *Chandra* is presented in Figure 6a. Again, the corresponding X-ray contours are overlaid on the  $H\alpha$  observation from *HST* in Figure 6b for a multiwavelength comparison. As seen for the *XMM-Newton* observation, the overall X-ray surface brightness distribution is similar to that in  $H\alpha$ , in agreement with earlier *Chandra* ACIS observations by Park et al. (2003). In particular, the ACIS observations show X-ray features which roughly correspond to the brightest groups of optical filaments, such as the SE ridge and the filaments that project from this region to the northwest and southwest. Similarly, the “patches” of optical emission on the western face of the remnant are accompanied by a minor X-ray enhancement in that region. The X-ray emission also outlines the optical cavity region, with the emission decreasing toward the interior of the region. Brighter X-ray emission traces the boundary with a radius of curvature similar to that expected from both the optical and echelle data. On the eastern and southern sides of the remnant, the faint X-ray extent matches very well the SNR boundary seen in diffuse  $H\alpha$  emission.

In addition to this morphological study, we examined the X-ray spectra using *XMM-Newton* data for three regions corresponding to significant optical features. These regions include one covering the SE Ridge of optical emission, one along the optically faint region in the northwest, and a third region corresponding to the cavity described in §4. For each region, spectra were extracted for each of the three *XMM-Newton* instruments (MOS1, MOS2, and pn) and fit jointly with spectral models for a thermal plasma modified by a model of photoelectric absorption.

The primary plasma model used is a plane-parallel shock, non-equilibrium ionization model (*vpshock* in XSPEC). This model presumes a simple shock structure with a constant postshock electron temperature  $kT$ . Ionization timescales are modeled as a broad distribution described by the ionization age  $\tau = n_e t_s$ , where  $n_e$  is the post-shock electron number density and  $t_s$  is the time since the plasma was shocked. This model provides a reasonable, if simplified, approximation to shocked plasma conditions for relatively high-temperature shocks in limited spatial regions of an SNR (Borkowski et al. 2001).

When describing broad spatial regions of an SNR, as we do here, one should keep in mind that the spectra arise from a range of temperatures and densities within that region. A single-temperature approximation is therefore of only limited utility in correctly describing the “characteristic” physical conditions. In many cases, it is necessary to use at least two linked models at different temperatures in order to better fit a spectrum which is in reality produced by a superposition of shocks in different conditions. However, particularly in smaller regions, too few counts are often present to constrain a large set of parameters,

as for instance those created by adding extra temperature components. The model fits are therefore a compromise: we use as few parameters as possible to characterize a given dataset, adding complexity as the number of counts increases sufficiently to require - and support - additional spectral components.

The best-fit spectral models for the SNR and for the selected spatial regions are given in Table 4. Listed in this table are the plasma model components used and the fitted values for absorption column density ( $N_H$ ), post-shock temperature ( $kT$ ), abundances of significant elements as a fraction of solar values ( $O/O_\odot$ , etc.); and ionization age ( $\tau$ ). Also listed are normalization values, proportional to the emission measure, for each of the *XMM-Newton* instruments ( $A_{MOS1}$ , etc). Finally, for each model fit the statistical goodness-of-fit values are given: reduced  $\chi^2$  ( $\chi^2_{\text{red}}$ ) and degrees of freedom (dof). Considering the associated errors and the lower spatial resolution of *XMM-Newton*, the results agree well with fits to *Chandra* ACIS data made by Park et al. (2003).

The X-ray spectra reflect the morphological differences between the eastern and western sides of the SNR. To the west, a single-component plasma model can adequately describe the spectrum. Likewise, the cavity region requires only a single plasma component for a reasonable fit. To the southeast, on the other hand, the spectrum requires two plasma components for a reasonable fit ( $\chi^2/\text{dof}=1122/743$ ). Notably, a combination of plasma and power-law components provides a considerably poorer fit ( $\chi^2/\text{dof}=1489/744$ ), allowing us to rule out, at the 90% confidence level, the possibility that the high-energy component of the spectrum is due to a nonthermal contribution.

Park et al. (2003) interpret this two-component fit to emission from the southeastern SNR as follows: the low-temperature component arising from the forward shock moving slowly into dense clouds, and the high-temperature component originating from the reheating of postshocked material by shocks reflected from dense clumps. Based on our velocity analysis, however, we suggest a slight modification of this picture. Rather than having two distinct temperature regimes, this region of the SNR, we suggest, is the location of a distribution of shock velocities. This picture is supported by the broad range of measured optical expansion velocities, as well as by the modelling of optical line emission by Vancura et al. (1992a). The two-temperature fit to the X-ray emission, therefore, can be regarded as an approximation to emission at a wide range of temperatures, generated by forward and reflected shocks at various speeds. These variations in local shock speed presumably arise from the encounter of the overall blast wave with material at different densities, as would be expected where the SNR is encountering the molecular cloud (Banas et al. 1997).

## 6. Summary

We have conducted a multiwavelength study of SNR N49 using *HST* images in  $H\alpha$ , [O III] and [S II] emission lines, archival *Chandra* and *XMM-Newton* images, and compared the morphological features to SNR kinematics, using the high-dispersion echelle spectra obtained at CTIO.

All emission line images reveal a highly filamentary morphology, with most prominent features being the SE Ridge, long filaments extending NW and a network of filaments in the SE. The optical emission from the western part of the remnant is significantly lower. We also detect a diffuse  $H\alpha$  emission component protruding beyond the shock boundary in all regions except for the west, where this emission is absent or undetected. We identify this diffuse component as the recombination radiation from the gas ionized by the UV precursor. Using  $H\alpha$  surface brightness, we have estimated the rms electron densities in different regions of the remnant.

Good correlation between [S II] and  $H\alpha$  morphology is demonstrated in the uniformity of the ratio map, with the mean value of  $0.75 \pm 0.05$ , and overall range of 0.4-1.4. [O III] images and a wide range of values on the [O III]/ $H\alpha$  ratio map manifest morphological differences between the [O III] and  $H\alpha$  emission. The most prominent feature, an offset between [O III] and  $H\alpha$  bright filaments, is demonstrated on the ratio map as an enhancement of [O III]/ $H\alpha$  ratio toward the outer edge of the image, where ratios reach between 0.8 and 1.5, with a few patches reaching up to 2.5. We observed the highest offset of  $0''.5$ . We propose that such an offset would arise in one of the two scenarios: (a) The offset is due to the thermal instabilities cushioned by magnetic fields and the associated secondary shocks. The fast shocks observed in N49 make this a likely scenario; however, a substantial amount of magnetic support is needed to account for the values of maximum observed offsets. (b) The offsets arise due to shocks propagating into a clumpy medium. The fast shocks just encountering the cloud produce the [O III] emission, while  $H\alpha$  comes from previously shocked clouds that have cooled sufficiently. The offset produced by this model matches the observations.

We have also carried out a detailed study of the remnant kinematics using high-dispersion echelle spectra at 7 different slit positions throughout the SNR. The spectra reveal a clumpy velocity structure, with discrete broad emission features matching well the positions of filaments across the slit, with radial velocity spreads reaching up to  $160 \text{ km s}^{-1}$ . We also detect a number of fainter clumps with very high radial velocity spreads that reach  $350 \text{ km s}^{-1}$ , and estimate the actual velocity of these clumps to be up to  $500 \text{ km s}^{-1}$ . In addition, we detect a narrow component extending throughout the slit, and we associate it with the diffuse  $H\alpha$  component identified morphologically.

We do not observe a bow-shaped signature of an expanding shell in the spectra. This indicates a true filamentary characteristic of the remnant and implies a clumpy structure of the gas surrounding the star prior to the explosion.

We also confirm the presence of the cavity in the remnant which matches the X-ray and radio data, and observe the asymmetric expansion of the gas in this region, which we associate with irregular density distribution of the surrounding matter prior to the explosion. Matching discrete emission features to actual filaments allows us to identify the blue- and redshifted filaments. Through a detailed comparison between the echelle spectra and the optical images, we have constructed a rough 3D map of the remnant.

We have compared the archival *Chandra* and *XMM-Newton* images to the  $H\alpha$  morphology. The X-ray morphology of N49 correlates well with the general trends seen in optical wavelengths. Even though we do not observe filamentary structure in X-rays, the brightest emission in X-rays comes from the SE, and the emission diminishes towards the west. The X-ray boundary matches the extent of optical filaments. Unlike in the optical, we observe the whole spherical envelope of the SNR in X-rays.

In addition to the images, we have carried out spectral analysis of the remnant. While the cavity region as well as the western side of the remnant can each be fit by a single plasma component, the eastern and SE regions require two component plasma. We rule out non-thermal radiation with 90% confidence. We suggest the 2 plasma component to be an approximation to a range of temperatures generated by forward and reflected shocks at various speeds.

The authors gratefully acknowledge the support of the Dean of the College of Liberal Arts and Sciences of the University of Illinois for YHC. RMW and YHC acknowledge support from STScI grant STI GO-8110. This material is based upon work supported by the National Aeronautics and Space Administration under grant NNG05GC97G issued through the Long-Term Space Astrophysics Program. We would like to thank the referee for useful suggestions to improve the paper.

Facilities: HST (WFPC2), CXO (ACIS), XMM (EPIC), Blanco.

## REFERENCES

- Banas, K. R., Hughes, J. P., Bronfman, L., & Nyman, L.-A. 1997, *ApJ*, 480, 607  
Blair, W. P., Sankrit, R., & Raymond, J. C. 2005, *AJ*, 129, 2268

- Borkowski, K. J., Lyerly, W. J., & Reynolds, S. P. 2001, *ApJ*, 548, 820
- Chu, Y.-H., & Kennicutt, R. C., Jr. 1988, *AJ*, 95, 1111
- Cox, D. P. 1972, *ApJ*, 178, 169
- Dickel, J. R., et al. 1995, *ApJ*, 448, 623
- Draine, B. T., & McKee, C. F. 1993, *ARA&A*, 31, 373
- Feast, M. 1999, *New Views of the Magellanic Clouds*, 190, 542
- Fender, R. P., Southwell, K., & Tzioumis, A. K. 1998, *MNRAS*, 298, 692
- Fesen, R. A., Blair, W. P., & Kirshner, R. P. 1982, *ApJ*, 262, 171
- Ghavamian, P., Hartigan, P., & Raymond, J. C. 2000, *ApJS*, 127, 323
- Innes, D. E. 1992, *A&A*, 256, 660
- Kulkarni, S. R., Kaplan, D. L., Marshall, H. L., Frail, D. A., Murakami, T., & Yonetoku, D. 2003, *ApJ*, 585, 948
- McCray, R., Kafatos, M., & Stein, R. F. 1975, *ApJ*, 196, 565
- McKee, C. F., & Ostriker, J. P. 1977, *ApJ*, 218, 148
- Park, S., Burrows, D. N., Garmire, G. P., Nousek, J. A., Hughes, J. P., & Williams, R. M. 2003, *ApJ*, 586, 210
- Rakowski, C. E., Raymond, J. C., & Szentgyorgyi, A. H. 2007, *ApJ*, 655, 885
- Raymond, J. C., Hartmann, L., Black, J. H., Dupree, A. K., & Wolff, R. S. 1980, *ApJ*, 238, 881
- Rotschild, R. E., Kulkarni, S. R., & Lingenfelter, R. E. 1994, *Nature*, 368, 432
- Shull, J. M., & McKee, C. F. 1979, *ApJ*, 227, 131
- Shull, P., Jr. 1983, *ApJ*, 275, 611
- Shull, P., Jr., Dyson, J. E., Kahn, F. D., & West, K. A. 1985, *MNRAS*, 212, 799
- Smith, I. A., et al. 1998, *Advances in Space Research*, 22, 1133
- STScI, 2001; *The Guide Star Catalog, Version 2.2 (GSC2.2)*

Vancura, O., et al. 1992, ApJ, 401, 220

Vancura, O., Blair, W. P., Long, K. S., & Raymond, J. C. 1992, ApJ, 394, 158

Williams, R. M., Chu, Y.-H., Dickel, J. R., Petre, R., Smith, R. C., & Tavaréz, M. 1999,  
ApJS, 123, 467

Table 1. Optical *HST* WFPC2 Observations

Observation	Date	Line	Filter	Exposure
1	2000 Jul 13	H $\alpha$ $\lambda$ 6563	F656N	$2 \times 500$ s
2	2000 Jul 14	[S II] $\lambda\lambda$ 6716,6731	F673N	$2 \times 600$ s
3	2000 Jul 14	[O III] $\lambda$ 5007	F502N	720+637+800 s

Table 2. CTIO 4m Echelle Observations

Observation	Date	Exposure	Location	Position Angle
E1986-1	1986 Nov 20	300 s	N49 pos 1	90
E1986-2	1986 Nov 20	300 s	N49 pos 2	90
E1986-3	1986 Nov 20	300 s	N49 pos 3	90
E1986-4	1986 Nov 20	300 s	N49 pos 4	90
E1986-5	1986 Nov 20	300 s	N49 pos 5	90
E1995-1	1995 Jan 19	$2 \times 600$ s	N49 IRS pos	42.5
E2000-1	2000 Dec 10	600 s	N49	90
E2000-2	2000 Dec 10	300 s	N49 south	90
E2000-3	2000 Dec 10	300 s	N49 south, 3''N	90

Table 3. X-ray fluxes for the regions normalized by area

	Area arcmin <sup>2</sup>	Avg. Flux ergs cm <sup>2</sup> s <sup>-1</sup>	Norm. Flux ergs cm <sup>2</sup> s <sup>-1</sup> arcmin <sup>2</sup>
SE Limb	.269	$2.23 \times 10^{-11}$	$8.3 \times 10^{-11}$
NW Limb	.300	$9.47 \times 10^{-12}$	$3.2 \times 10^{-11}$
Cavity	.097	$9.54 \times 10^{-12}$	$9.8 \times 10^{-11}$

Table 4. Best-fit spectral models to XMM data for N49 and sub-regions

Parameter	Whole SNR		SE Limb		NW Limb	Cavity
component	vpshock + vpshock		vpshock + vpshock		vpshock	vpshock
$N_{\text{H}}$ ( $\text{cm}^{-2}$ )	$2.9^{+0.1}_{-0.1} \times 10^{21}$		$3.2^{+0.3}_{-0.3} \times 10^{21}$		$2.3^{+0.1}_{-0.1} \times 10^{21}$	$2.2^{+0.1}_{-0.1} \times 10^{21}$
$kT$ (keV)	$0.41^{+0.01}_{-0.01}$	$0.98^{+0.01}_{-0.01}$	$0.40^{+0.03}_{-0.03}$	$1.02^{+0.01}_{-0.03}$	$0.66^{+0.01}_{-0.02}$	$0.54^{+0.01}_{-0.01}$
$O/O_{\odot}$	$0.24^{+0.01}_{-0.01}$		$0.21^{+0.01}_{-0.01}$		$0.65^{+0.05}_{-0.05}$	$0.38^{+0.03}_{-0.03}$
$\text{Ne}/\text{Ne}_{\odot}$	$0.31^{+0.01}_{-0.01}$		$0.29^{+0.01}_{-0.02}$		$0.62^{+0.06}_{-0.05}$	$0.38^{+0.04}_{-0.02}$
$\text{Mg}/\text{Mg}_{\odot}$	$0.31^{+0.01}_{-0.02}$		$0.25^{+0.02}_{-0.03}$		$0.30^{+0.06}_{-0.01}$	$0.23^{+0.03}_{-0.03}$
$\text{Si}/\text{Si}_{\odot}$	$0.57^{+0.02}_{-0.02}$		$0.65^{+0.05}_{-0.04}$		$0.41^{+0.05}_{-0.06}$	$0.48^{+0.08}_{-0.04}$
$\text{S}/\text{S}_{\odot}$	$0.67^{+0.05}_{-0.05}$		$0.9^{+0.1}_{-0.1}$		$0.7^{+0.2}_{-0.2}$	$1.1^{+0.5}_{-0.1}$
$\text{Fe}/\text{Fe}_{\odot}$	$0.34^{+0.01}_{-0.01}$		$0.34^{+0.01}_{-0.02}$		$0.24^{+0.01}_{-0.02}$	$0.16^{+0.01}_{-0.02}$
$\tau$ ( $\text{cm}^{-3}$ s)	$3.1^{+0.1}_{-0.3} \times 10^{11}$	$> 1.0 \times 10^{13}$	$2.8^{+0.4}_{-0.2} \times 10^{11}$	$> 1.2 \times 10^{13}$	$9^{+1}_{-1} \times 10^{11}$	$1.2^{+0.2}_{-0.1} \times 10^{12}$
$A_{\text{MOS1}}$ ( $\text{cm}^{-5}$ )	$4.8^{+0.1}_{-0.1} \times 10^{-2}$	$1.6^{+0.1}_{-0.1} \times 10^{-2}$	$2.8^{+0.5}_{-0.4} \times 10^{-2}$	$6.2^{+0.3}_{-0.2} \times 10^{-3}$	$5.9^{+0.1}_{-0.2} \times 10^{-3}$	$9.3^{+0.4}_{-0.3} \times 10^{-3}$
$A_{\text{MOS2}}$ ( $\text{cm}^{-5}$ )	$5.6^{+0.1}_{-0.1} \times 10^{-2}$	$1.6^{+0.1}_{-0.1} \times 10^{-2}$	$3.0^{+0.5}_{-0.4} \times 10^{-2}$	$6.0^{+0.3}_{-0.3} \times 10^{-3}$	$6.3^{+0.2}_{-0.2} \times 10^{-3}$	$1.0^{+0.1}_{-0.1} \times 10^{-2}$
$A_{\text{pH}}$ ( $\text{cm}^{-5}$ )	$5.8^{+0.1}_{-0.1} \times 10^{-2}$	$1.6^{+0.1}_{-0.1} \times 10^{-2}$	$3.1^{+0.4}_{-0.3} \times 10^{-2}$	$6.8^{+0.2}_{-0.3} \times 10^{-3}$	$6.3^{+0.3}_{-0.1} \times 10^{-3}$	$1.0^{+0.1}_{-0.1} \times 10^{-2}$
$\chi_{\text{red}}^2$	2.13		1.54		1.32	1.56
dof	875		625		485	435

Note. — Spectra cover the range between 0.3-8.0 keV.  $A$  is the normalization constant, defined as  $A = 10^{-14} \int n_e n_H dV / (4\pi D^2)$ , where  $n_e$  and  $n_H$  are electron and proton densities, respectively, and  $D$  is the distance, all in cgs units. Elements not listed are fixed to the LMC mean abundance. Errors give the 90% confidence range for each fit parameter. Errors in  $N_{\text{H}}$ ,  $kT$ ,  $\tau$  and  $A$  are estimated with all abundances except Fe fixed at their best-fit values; abundance errors are estimated with  $N_{\text{H}}$ ,  $kT$  and  $\tau$  fixed.

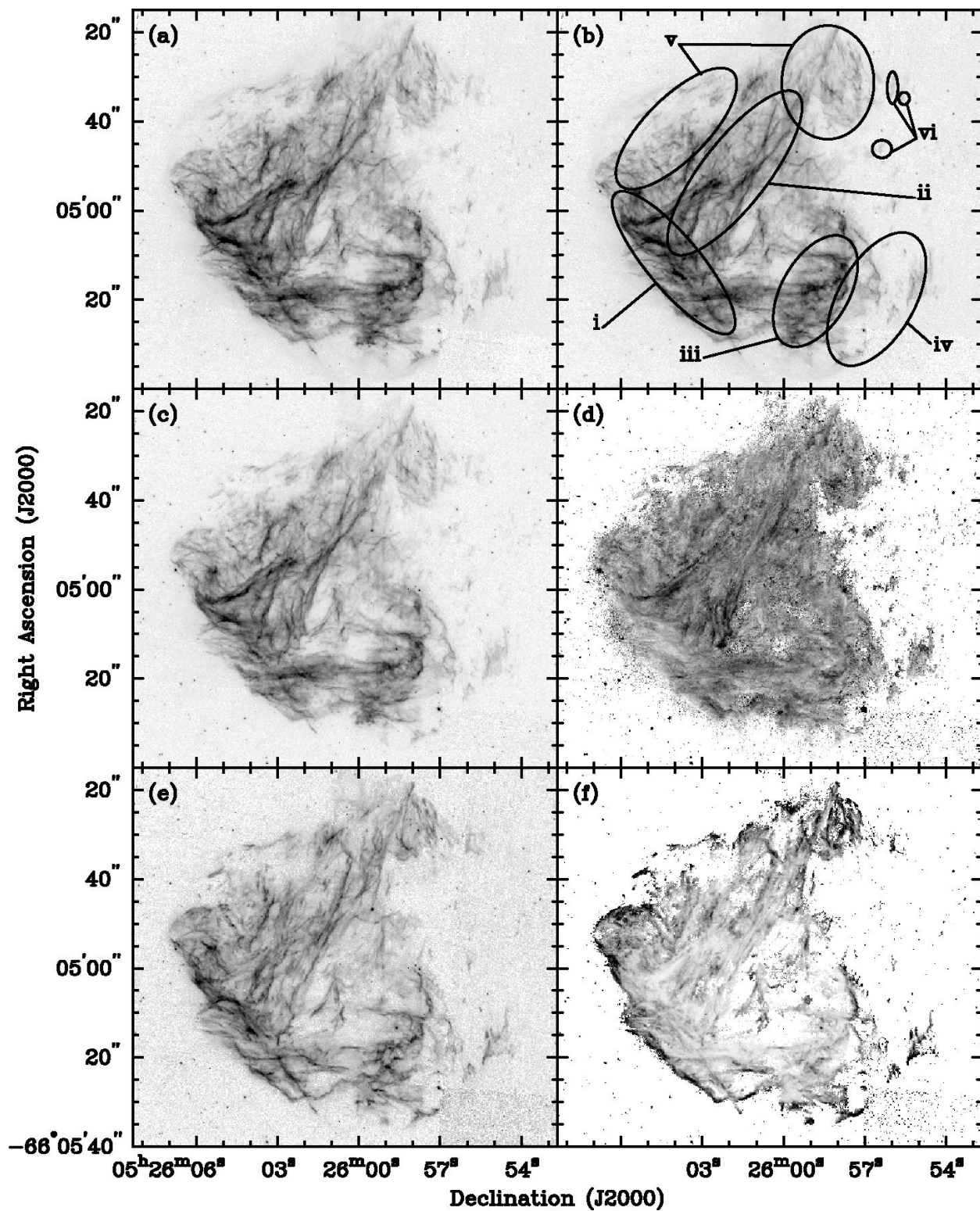


Fig. 1.— Mosaicked and flux-calibrated *HST* WFPC2 images and ratio maps of N49 displayed in linear greyscale. The panels are (a) H $\alpha$  image, (b) morphological features marked on the H $\alpha$  image, (c) [S II] emission line image, (d) [S II]/H $\alpha$  ratio map, (e) [O III] emission line image, (f) [O III]/H $\alpha$  ratio map.

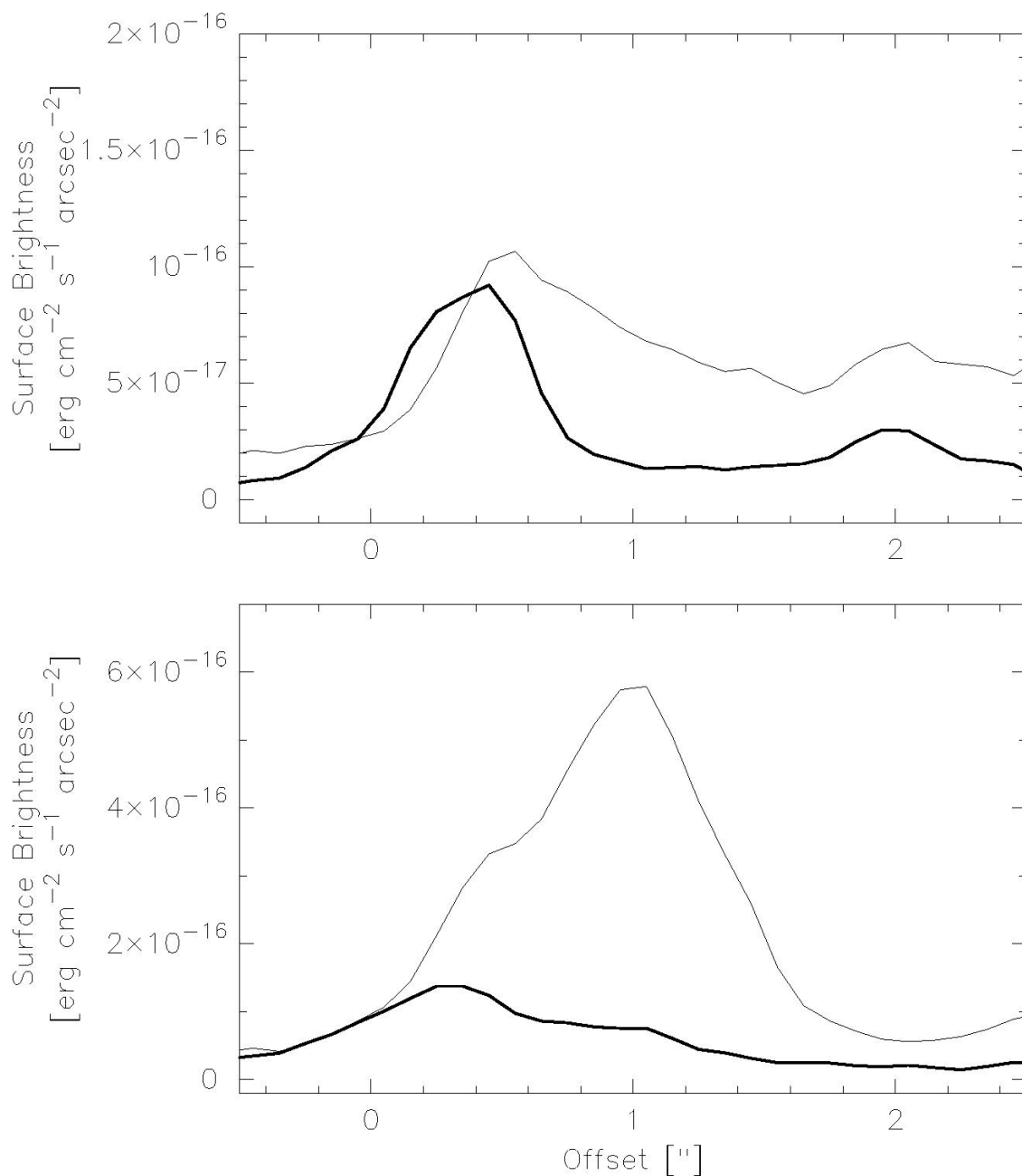


Fig. 2.— Surface brightness profiles of H $\alpha$  (thin line) and [O III] (thick line) emission across selected filaments. The coordinates for the positions marked as zero are 05<sup>h</sup>26<sup>m</sup>01<sup>s</sup>.34, –66°05′29″.1 (J2000), at PA = 30° for the top panel, and 05<sup>h</sup>26<sup>m</sup>04<sup>s</sup>.4, –66°05′18″.7 (J2000) at PA = 135° for the bottom panel.

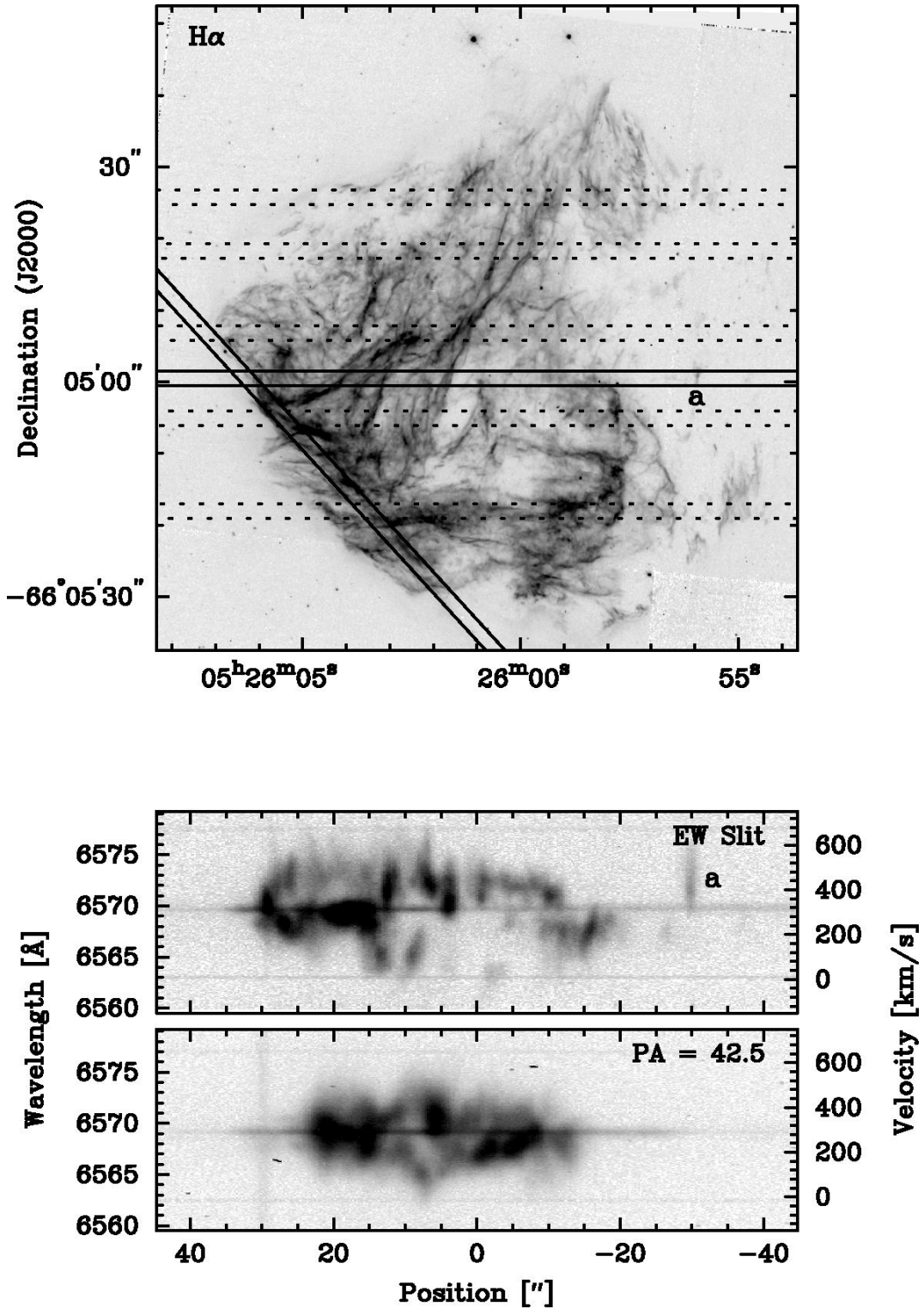


Fig. 3.— Echellograms of N49 for E2000-1 and E1995-1 data, with corresponding positions on the  $H\alpha$  image marked by the solid horizontal and tilted lines, respectively. The feature a in the E2000-1 echelle spectrum and the optical image is a high-velocity clump discussed in §4.1. The dashed lines mark the positions of E1986-1, -2, -3, -4 and -5 (bottom to top) spectra taken by Chu & Kennicutt (1988).

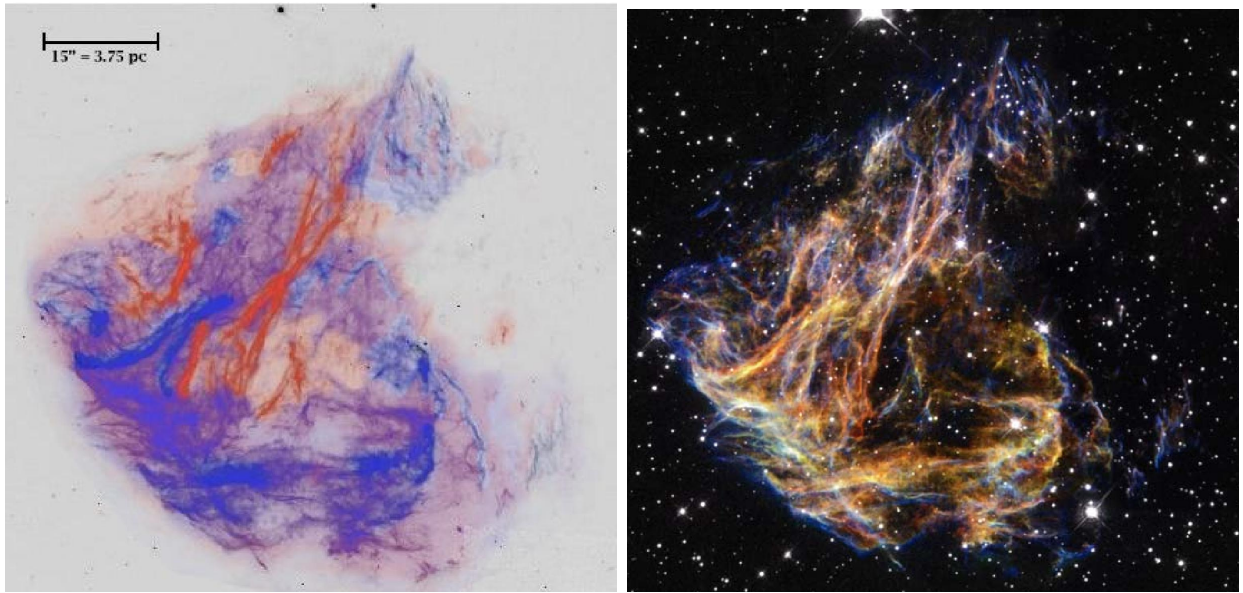


Fig. 4.— (a) A 3D cartoon of N49 with blue and red filaments corresponding to the near and the far side of the remnant, respectively. (b) An overlay *HST* image of  $H\alpha$  (red), [S II] (yellow) and [O III] (blue) emission.

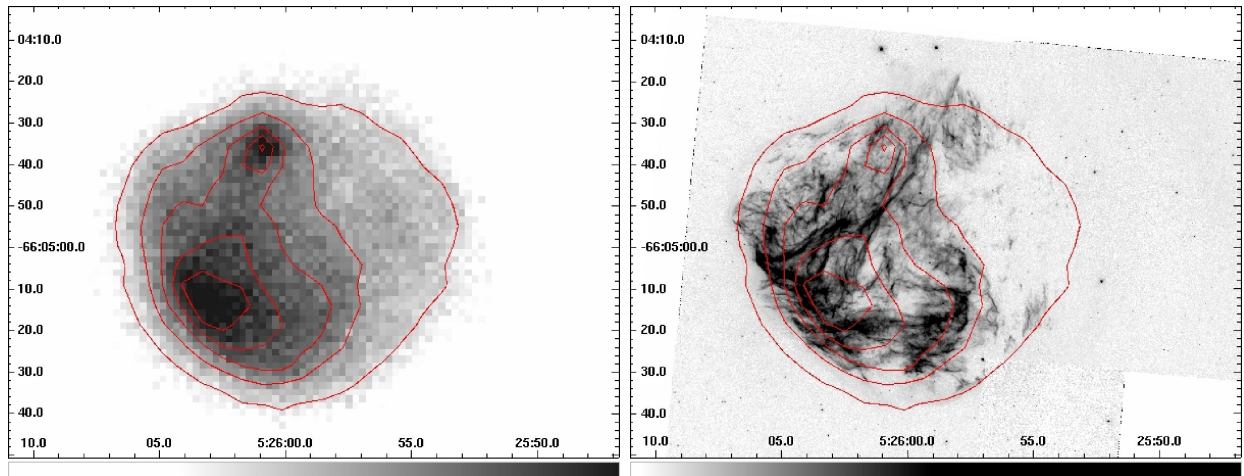


Fig. 5.— (a) Smoothed contours of *XMM-Newton* X-ray data; (b) The same *XMM-Newton* contours overlaid on the optical  $H\alpha$  image from *HST*. This image was binned in pixels of  $1''.6 \times 1''.6$ . Contours plotted on the image range from  $3\sigma$  –  $30\sigma$  above the background in 5 evenly spaced linearly increasing contours.

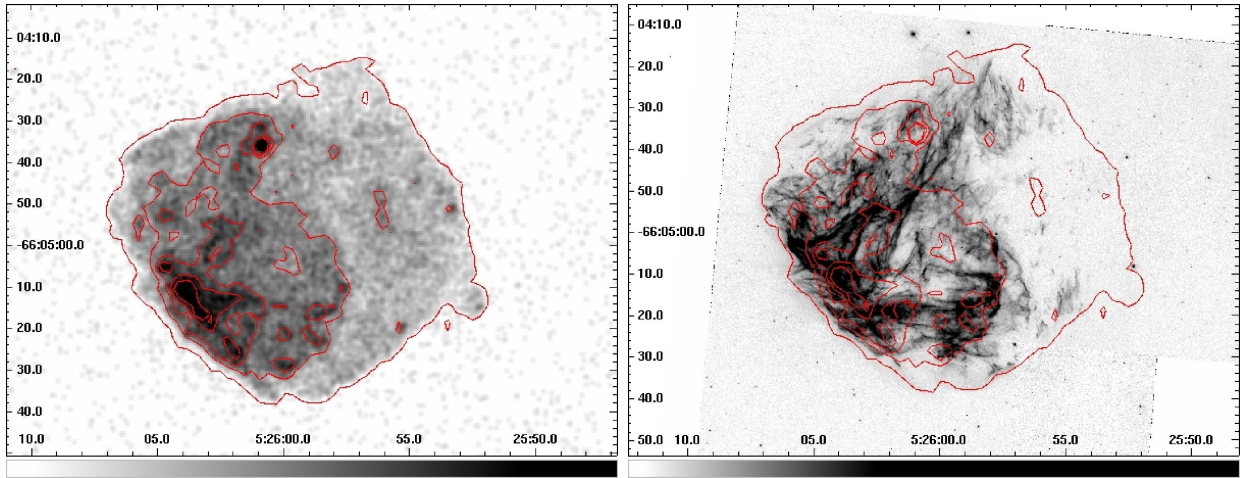


Fig. 6.— (a) Smoothed contours of *Chandra* ACIS X-ray data; (b) The same contours overlaid on the optical H $\alpha$  image from *HST*. This image was processed with a 2 pixel gaussian smoothing. Contours plotted on the image range from  $2\sigma$  –  $100\sigma$  above the background in 5 evenly spaced linearly increasing contours.